Analysis of Different Computational Techniques for Calculating the Polarizability Tensors of Stem Cells With Realistic Three-Dimensional Morphologies

Somen Baidya, Ahmed M. Hassan, *Member, IEEE*, Waleed Al-Shaikhli, Beatriz A. Pazmiño Betancourt, Jack F. Douglas, and Edward J. Garboczi

***Abstract*—Recently, the National Institute of Standards and Technology has developed a database of three-dimensional (3-D) stem cell morphologies grown in ten different scaffolds to study the effect of the cells' environments on their morphologies. The goal of this paper is to study the polarizability tensors of these stem cell morphologies, using three independent computational techniques, to quantify the effect of the environment on the electric properties of these cells. We show excellent agreement between the three techniques, validating the accuracy of our calculations. These computational methods allowed us to investigate different meshing resolutions for each stem cell morphology. After validating our results, we use a fast and accurate Padé approximation formulation to calculate the polarizability tensors of stem cells for any contrast value between their dielectric permittivity and the dielectric permittivity of their environment. We also performed a statistical analysis of our computational results to identify which environment generates cells with similar electric properties. The computational analysis and the results reported herein can be used for shedding light on the response of stem cells to electric fields in applications such as dielectrophoresis and electroporation and for calculating the electric properties of similar biological structures with complex 3-D shapes.**

***Index Terms*—Cell morphology, finite element method, polarizability, stem cells, surface integral equation, minimum enclosing ellipse.**

Manuscript received June 25, 2018; revised September 19, 2018; accepted October 9, 2018. Date of publication October 15, 2018; date of current version June 21, 2019. This work was supported in part by the NIST Grant 70NANB15H285 and in part by the University of Missouri-Kansas City, School of Graduate Studies Research Award. *(Corresponding author: Ahmed M. Hassan.)*

S. Baidya and W. Al-Shaikhli are with the Department of Computer Science and Electrical Engineering, University of Missouri–Kansas City.

A. M. Hassan is with the Department of Computer Science and Electrical Engineering, University of Missouri–Kansas City, Kansas City, MO 64110 USA (e-mail: hassanam@umkc.edu).

B. A. P. Betancourt and J. F. Douglas are with the Materials Science and Engineering Division, Material Measurement Laboratory, National Institute of Standards and Technology.

E. J. Garboczi is with the Applied Chemicals and Materials Division, Material Measurement Laboratory, National Institute of Standards and Technology.

Digital Object Identifier 10.1109/TBME.2018.2876145

I. Introduction

ACCURATE characterization of a cell's morphology is crucial in many applications such as quantifying cellular responses under the influence of extracellular signals [1]. This is why morphological cell analysis has proved to play a significant role in many applications of biomedical engineering. Cytopathology or the science of diagnosis based on a single cell or a cell cluster is established on the subjective interpretation of cell morphological features by cytopathologists [2]. These morphological characteristics have numerous applications [3]–[11]. For example, cancerous cells exhibit micro-morphological changes through the different stages of tumorigenesis [3], apoptosis [4], cell division, and proliferation [5]. These changes can be detected by comparing the morphological features of normal cells with that of the cancerous cells at different stages, and hence open up a broad field of early cancer detection. Physiological fluctuations in reproductive function or cell classification based on their functionality can also be achieved by quantifying the morphological characteristics of a cell [6]–[8]. Dynamic feature extraction, to dissect cellular heterogeneity or the development of new drugs are other examples of applications that utilize the cell's morphological characteristics [9], [10]. As a result, cell imaging is an essential analysis tool in the field of cell cytology, neurobiology, pharmacology and biomedical research disciplines [11].

The physical interactions between the cell and the extracellular environment, in which the cells are embedded, have a significant effect on the shape of the cell [12]. Recent advancement in three-dimensional microenvironment engineering have enabled researchers to mimic the real *in vivo* conditions [13]–[15]. By engineering the biomaterial scaffold culture, researchers have been able to achieve desired cell shapes and hence control the cell's functionality [16]–[19]. Culturing the same cell in different biomaterial scaffolds leads to variation in the cell morphology. Florczyk *et al*. referred to this as cellular morphotyping, where they incorporated a cell line of human bone marrow stromal cells (hBMSCs) cultured in different microenvironments [20]. The present study draws upon on a database, recently developed by the *National Institute of Standards and Technology* (NIST), consisting of the 3D surface and volumetric map of stem cells

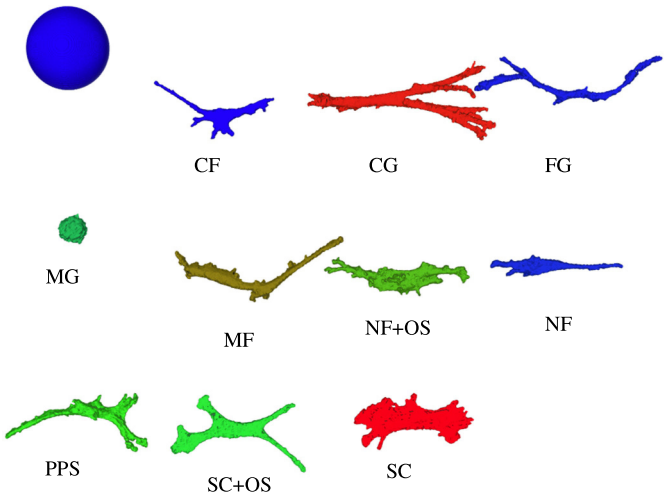

Fig. 1. Morphological depiction of ten different cells from each family made to be approximately to scale to illustrate the differences in geometric features between the different shapes. The abbreviations for each type are explained in Section II-A. The blue sphere in the upper left corner serves as a size scale of 100 μm diameter sphere. The color depiction is such that red has the larger volumes; blue is the lower volumes, and green shows intermediate volumes.

grown in different environments. The motivation behind developing that database was to shed light upon the effect of the cell's microenvironment on its 3D morphological features [21]. The database is accessible via an open source interactive user interface [22] and available in *.obj* (wavefront) format and volumetric mesh format (*voxels*) for future studies [23]. The cells were divided into ten groups based on the microenvironments in which they were grown. Microenvironments with different geometrical and/or chemical properties were constructed to guide the cell's morphology to have characteristic shapes such as elongated, columnar, or equi-axial shapes [24]. The cells were imaged using confocal laser scanning microscopy, which generated a stack of 2D slices or cross sections for each cell [25]. The substantial number of 2D images (z-stacks) were then categorized as foreground or background by applying an automated segmentation algorithm. The wide variability in cell morphologies was introduced by carefully engineering the scaffolds, where the stem cells were grown, to mimic different natural environments for the stem cells. Fig. 1 shows one cell from each of the ten families studied in the database. As shown in the figure, the cells exhibit a wide range of variation in morphology. For example, one cell morphology has an equi-axial sphere-like distribution (MG) whereas another cell is distributed along only one axis and is more similar to a 1D rod like structure (NF).

Florczyk *et al*. incorporated 82 different shape measures to assess the effect of the environment on the morphological features of the cell [20]. For determining cellular dimensionality, they organized the cells in a cellular dimensionality plot where each cell is assigned a coordinate based on ratios of elements in its radius of gyration tensor. The relative location of each cell in this dimensionality plot defines the cell's properties and allows us to predict the scaffold's characteristics. For example, the question of whether the culturing medium is flat (2D) or whether it possesses 3D features or pores can be assessed from the smallest element of the gyration tensor. For a cell cultured on a 3D substrate, the smallest gyration tensor element was much larger than that of cells cultured on a 2D substrate, which would cause one diagonal element to be close to zero. *Hierarchical Cluster Analysis* (HCA) and *Principle Component Analysis* (PCA) were also incorporated for the statistical analysis of the dimensionality data [20]. However, the PCA and HCA analysis were incapable of identifying the scaffold of single cells due to the large heterogeneity in the cell shapes and the resulting heterogeneity in the dimensionality data.

Betancourt *et al*. recently employed the numerical path integrator ZENO to calculate the DC electric polarizabilities of the stem cells from the same database [24]. ZENO uses random walks to calculate the electric polarizability, capacitance and intrinsic viscosity of arbitrary shaped particles [26], [27]. The mathematical foundation of ZENO's random walk calculations automatically assign infinite contrast to the studied particle. That is, the polarizability of objects with arbitrary contrast cannot be calculated using ZENO. Therefore, the study of Pazmiño *et al*. only considers the electric polarizability tensor, the limiting situation in which stem cells are assumed to be perfect conductors. The reported results provide insight into how the local microenvironment of cells can influence how they react to an electric field stimulus. However, *in vitro* studies and several numerical studies emphasizes that we should incorporate non-ideal cases in cell polarizability studies [28]–[32]. For example, Sebastián *et al*. employed an adaptive finite element numerical approach to calculate the complex polarizability of realistic red blood cells by calculating the electric field distribution inside the membrane and using the effective dipole element method [33]. They concluded that the polarizability of the cell calculated using anisotropic properties can be significantly different from that of the cell calculated using isotropic properties. They also used the same approach to determine the complex polarizability of four types of hematic cells: *T-lymphocytes*, *platelets*, *erythrocytes*, and type-II *stomatocytes* [31]. Prodan *et al*. developed a theoretical framework to explain the accumulation of surface charge over the cell membrane boundary in suspension (i.e., known as α- *relaxation* process in $<$10 kHz range and β- *relaxation* process at higher frequencies) by calculating the complex polarizability of a single shelled spherical cell (shell representing the membrane) [32]. Di Biasio *et al*. extended the polarizability expression to account for shape variability (i.e., ellipsoidal, toroidal) [29], [30]. Experimental validation of their model was presented by studying the low-frequency dielectric dispersion (α- *dispersion*) of *E. coli* bacteria cell in suspension [28].

For a more accurate assessment of the stem cells' response to an electric stimulus, computational techniques need to be developed that can calculate the polarizability of these complex stem cells using their true electrical properties. Moreover, since no closed form expressions exist for the polarizability of these complex-shaped stem cells, multiple independent computational techniques need to be tested to validate the accuracy of the calculated polarizabilities. The stem cells database provided at least five different representations for each cell with different resolutions. The resolution varied from the highest value,

obtained directly from the raw confocal microscope images, down to the lowest value, which was 16 times coarser than the original value (details below). The highest resolution provides the most accurate representation of the true shape of the stem cell. However, it contains an extremely large number of discretization elements that can lead to prohibitively large computational time in some numerical techniques. In most of the reported numerical experiments, the representations with moderate resolution were used to describe the stem cells [24].

The goal of this work is to extend these recent studies by addressing these challenges. Due to the complexity of the morphologies of these cells, we have incorporated three independent computational methods to calculate the polarizability tensors and validated our result through the excellent agreement in the numerical results achieved by the three techniques. We also adapted these computational techniques to calculate the polarizability tensors of the stem cells at an arbitrary contrast between their electric properties and the electric properties of the environment. This allows us to predict more accurately the response of stem cells, with realistic electric properties, to an arbitrary electric stimulus. After validating our calculations, we quantified the relationship between the polarizability tensors and the cell shapes. We also clarified the variations in the polarizability values with the variations in the meshing resolution used to describe each stem cell. Finally, we used a simple Páde approximation technique that employs the numerical results in two cases of extreme electrical contrast between a cell and its environment to calculate, with high accuracy, the polarizability tensors of stem cells with uniform but arbitrary electrical properties.

This paper is arranged as follows: In Section II, we briefly describe the NIST stem cells database and the various microenvironments used to generate this database, we briefly introduce the theory behind the static polarizability calculation, and we describe the three numerical techniques employed in this work. In Section III, we present the polarizability results obtained from the different solvers. These results are discussed and conclusions drawn in Sections IV and V respectively.

II. Methodology

A. NIST 3D Stem Cell Database

In the NIST stem cell database, ten different scaffold families were employed [20], [21]. The scaffold families can be divided into five major categories based on their geometry and material composition (all names taken from the NIST database):

1) Spun-Coat (SC), Nanofiber (NF), and Microfibers (MF): Spun-Coat (SC), Nanofiber (NF), and Microfibers (MF) scaffolds were made from the poly(ε-caprolactone) (PCL) polymer. The Spun-Coat scaffold was composed of flat films of PCL that provided a 2D environment. The Nanofiber and Microfiber scaffolds consisted of electrospun fibers with different sizes creating a complex porous 3D environment. The fibers in the Nanofiber category had a diameter of 589 nm and the fibers employed in the Microfiber category were 4.4 μm in diameter [20], [21].

2) Matrigel (MG), Collagen Gel (CG), and Fibrin Gel (FG): Matrigel (MG), Collagen Gel (CG), and Fibrin Gel (FG) scaffolds were composed of hydrogels obtained from three different natural sources. Fibrin Gel was composed of fibrinogen obtained from human plasma and Collagen gel was obtained from bovine Type I collagen [20], [21]. Matrigel scaffolds were obtained from the secretions of mice sarcoma cells. These three families formed porous 3D environments for the stem cells.

TABLE I
Identifiers of the Ten Cell Shapes Used in This Study

Scaffold Environment	Cell Identifier
SC	080613_SJF_SC1_d1_63x_12
NF	080713_SJF_NF1_d1_63x_18
MF	012014_SJF_BigNF_1d_63x_25
MG	022614_SJF_Matrigel_1d_63x_05
CG	050214_SJF_Collagen Gel_1d_63x_02
FG	040114_SJF_Fibrin Gel_1d_63x_07
CF	010914_SJF_Coll_Fibrils_1d_63x_2_05
SC+OS	091313_SJF_SC+OS_d1_63x_18
NF+OS	091613_SJF_NF+OS_d1_63x_08
PPS	012314_SJF_Alvetex_1d_63x_13

3) Collagen Fibrils (CF): Collagen Fibrils (CF) scaffolds were obtained from bovine collagen similar to Collagen Gel. However, Collagen Gel was allowed to form a 3D porous gel structure whereas collagen fibrils were confined to a 2D film forming 200 nm diameter collagen fibers [20].

4) Spun-Coat + Osteogenic Supplements (SC+OS) and Nanofiber + Osteogenic Supplements (NF+OS): Spun-Coat + Osteogenic Supplements (SC+OS) and Nanofiber + Osteogenic Supplements (NF+OS) scaffolds were geometrically identical to the SC and NF scaffolds, respectively. However, Osteogenic Supplements were added to the SC and NF scaffolds to form the SC+OS and NF+OS scaffolds. Therefore, by comparing the stem cells grown in the SC+OS scaffolds with the stem cells grown in the SC scaffolds, we can assess whether the chemical composition of the environment has an effect on cell shape or whether the geometry of the environment is the sole regulator of cell shape [20], [21].

5) Porous Polystyrene Scaffold (PPS): Porous Polystyrene Scaffold (PPS) scaffolds were composed of polystyrene and they represent one of the most commonly used 3D cell cultures [20], [21]. Unlike the NF and MF scaffolds, PPS is not composed of cylindrical fibers but is typically composed of more flattened ribbons. In PPS scaffolds, the pores range from 36 μm to 40 μm [20].

Approximately 100 different stems cells were imaged from each environment. Each cell was provided with a unique identifier. We started our numerical experiments by studying ten different cell shapes, one cell shape from each of the ten environments. The identifiers of the selected stem cells are summarized in Table I and taken from [20].

Each cell was stained for actin and nucleus for obtaining the morphology of cell cytoplasm and nucleus separately [20], [23]. Both the cell cytoplasm and the nucleus shape data are available in two different formats for user convenience: *(i)* the original voxel representation of the segmented cell image and *(ii)* triangular surface mesh representation obtained via the Marching Cubes algorithm from the original voxel representation and

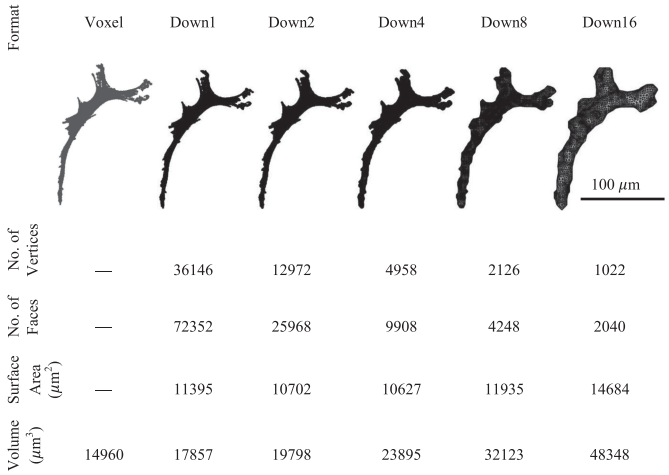

Fig. 2. Illustration of the raw voxels and the five different surface meshes of a PPS cell down sampled by factors from 1 to 16. As the resolution decreases, the volume increases from 17857 μm^3 ("down1") to 48348 μm^3 ("down16"), a factor of about 2.7, while the surface area increases more slowly, from 11395 μm^2 to 14684 μm^2. In addition, the number of face and vertices decrease from "down1" to "down16", losing sharpness and some features of the original shape.

down-sampled representations. The triangular mesh representation is available in five different versions, each version down-sampled by a factor that ranges from 1 to 16 in powers of two [23]. For example, the "*down4*" mesh was generated by first representing each 4 pixels of the original cell morphology in each image in the stack of images defining the cell with one larger pixel, then operating with the Marching Cubes algorithm. Clearly, the "*down1*" mesh was generated from the original unchanged voxels. Fig. 2 depicts how down-sampling affects the actual morphology of a particular cell (in this case PPS). As can be observed from Fig. 2 and the associated data, down sampling the original mesh decreases the resolution of the original morphology and increases the stem cell's volume and surface area.

B. Theory of Electrostatic Polarizability

The inclusion of an isotropic or anisotropic particle in a homogenous environment, excited by a uniform electric field, will perturb this electric field in the vicinity of the inclusion [34]. The incident electric field will lead to the separation of charges on the surface of the particle, creating an overall dipole moment. The ratio between the induced dipole moment, p, and the incident electric field, E, is defined as the polarizability (α) of the particle. The polarizability α is a direct function of the shape, the electric properties of the particle, and the electric properties of the environment where the particle is embedded. Closed form expressions for the polarizability of simple shapes, like spheres and ellipsoids, are relatively easy to obtain because of the uniform distribution of the internal field [35], [36]. However, for stem cells with complex 3D geometries, the polarizability calculation is only possible via a numerical solution of the Laplace equation [34] (depicted in (1)):

$$\nabla^2 \phi\,(r) = 0 \tag{1}$$

In (1), ϕ is a sum of the incident potential ϕ_e and the perturbed potential caused by the presence of the particle. For a randomly oriented inclusion with no planes of symmetry, the polarizability tensor will have in general nine non-zero elements, α_{ij}. However, the polarizability tensor is symmetric with a maximum of six independent components. By using matrix diagonalization, we can obtain the diagonalized form of the tensor (as shown in (2)), which can be achieved when the major axes of the particle are aligned with the principal axes of the coordinate system, x, y, and z [37].

$$\alpha = \begin{bmatrix} \alpha_{xx} & \alpha_{xy} & \alpha_{xz} \\ \alpha_{yx} & \alpha_{yy} & \alpha_{yz} \\ \alpha_{zx} & \alpha_{zy} & \alpha_{zz} \end{bmatrix} \quad \overrightarrow{Diagonalization}$$
$$\hat{\alpha} = \begin{bmatrix} \hat{\alpha}_{xx} & 0 & 0 \\ 0 & \hat{\alpha}_{yy} & 0 \\ 0 & 0 & \hat{\alpha}_{zz} \end{bmatrix} \tag{2}$$

Some symmetrical morphologies will have degenerate diagonal components, e.g., $\hat{\alpha}_{xx} = \hat{\alpha}_{yy}$. However, the following analysis will be the same. Theoretically, the polarizability of a particle for arbitrary values for ϵ_p and ϵ_m can be calculated using (3) [34]:

$$\alpha_{ij} = \left(\frac{\epsilon_p}{\epsilon_m} - 1\right) \int_V \hat{j}.E_i dV \tag{3}$$

where, j is selectively varied to x, y, and z based on the polarizability element of interest, i is determined by the direction of the incident field, and V is the volume of the inclusion. Different components of the polarizability tensor can be calculated by varying the direction of the incident electric field and by selecting different components of the electric field inside the particle E_{i}. The electric polarizability tensor, $[\alpha_E]$, can be calculated by assigning infinity to the relative permittivity of the particle ($\epsilon_{\mathrm{p}} = \infty$). For the case of a perfect conductor, the electric field is normal to the surface of the particle, see Fig. 3(a), and the electric field inside the particle diminishes to zero. This will make the integral in (3) undefined and, therefore, the surface integral form of (3) is preferred for calculating α_{ij} for the case of $\epsilon_p = \infty$ [37].

The magnetic polarizability tensor, $[\alpha_{\mathrm{M}}]$, can also be calculated using (3) by assigning zero to the relative dielectric permittivity of the particle ($\epsilon_{\mathrm{p}} = 0$). As shown in Fig. 3(b), this ϵ_{p} choice diminishes the normal component of the electric field at the surface of the particle but the tangential field component will be then non-zero. Since (3) does not have a closed form solution for particles with complex shapes, different numerical techniques need to be employed to validate each other.

1) COMSOL Mulstiphysics[1]: COMSOL is a commercial multi-physics software package that uses the Finite Element Method (FEM) to calculate the desired physical properties [38].

[1]Certain commercial equipment and/or materials are identified in this report in order to adequately specify the experimental procedure. In no case does such identification imply recommendation or endorsement by the National Institute of Standards and Technology, nor does it imply that the equipment and/or materials used are necessarily the best available for the purpose.

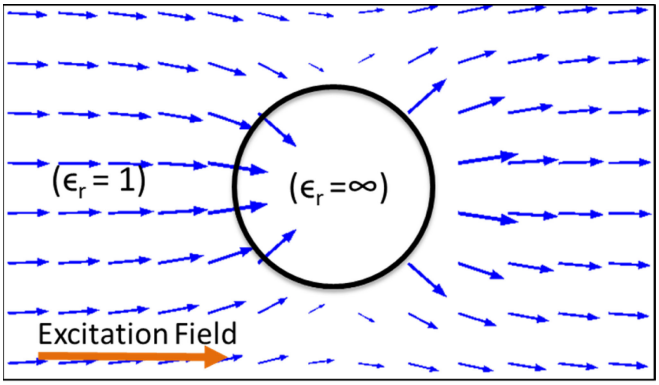

(a) Perfect Electric Conductor

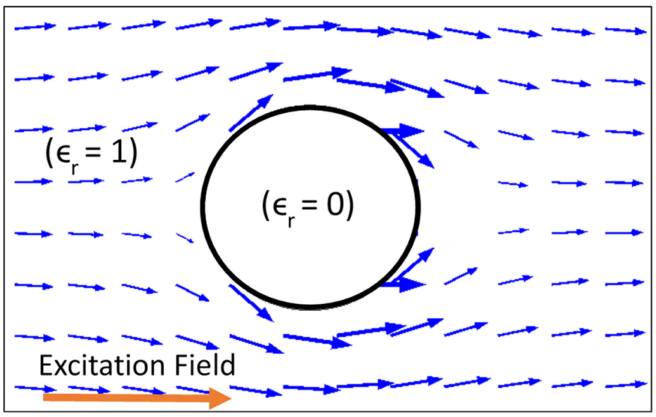

(b) Perfect Magnetic Conductor

Fig. 3. Electric field distribution along the surface of a body with (a) perfect electric conductor (PEC), (b) perfect magnetic conductor (PMC) properties. For PEC, at the surface only normal fields exist whereas in case of PMC the field lines are tangential only at the surface.

FEM solvers like COMSOL require the geometry of interest to be subdivided into smaller volumetric elements (e.g., tetrahedrals, pyramids, or prisms) and solves the desired equations at every volumetric element under appropriate boundary conditions [38]. In this work, we used the Electrostatics physics interface under the AC/DC COMSOL module for our problem definition. This module uses FEM to solve Maxwell's equations under the static approximation [39]. The stem cell database contains the surface mesh of each cell morphology in the wavefront *.obj* format. We converted the cell mesh into STL (*STereoLithography*) format using MeshLab [40] to facilitate the import of the cells' geometries into COMSOL. COMSOL uses this STL mesh to define the surface or the outer boundary of the stem cell. COMSOL would then mesh the volume enclosed by this surface into volumetric tetrahedral elements [39]. To ensure the accuracy of the imported mesh, we validated that the number of faces in the outer surface of the stem cell did not change from the original values after it was imported to COMSOL. We also confirmed that the volume of the imported cell calculated by COMSOL matched the original volume of the cell as calculated by MeshLab. The cells were embedded in a large sphere whose radius was at least 25 times the size of the imported cell to replicate free space conditions. The medium enclosed by that bounding sphere was assigned a relative permittivity of unity, $\epsilon_{\mathrm{m}} = 1$, and the material inside the cell was assigned a variable permittivity ϵ_{p} based on the polarizability tensor of interest.

2) Scuff-EM: Scuff-EM (Surface CUrrent/Field Formulation of ElectroMagnetism) is an open source Method of Moment (MoM) solver for static and dynamic electromagnetic scattering [41]. Scuff-EM requires the particles to be represented in .msh format which can be generated from the STL representation of the stem cells using the open source mesh generator Gmsh [42]. *Scuff-Static* is the static subroutine in the Scuff-EM package and the fundamental equation for this subroutine is depicted in (4) below:

$$\emptyset\left(\boldsymbol{r}\right) = \emptyset^{ext}\left(\boldsymbol{r}\right) + \frac{1}{4\pi\epsilon_0}\sum_s \oiint \frac{1}{|\boldsymbol{x}-\boldsymbol{x}'|}\sigma(\boldsymbol{r}')d\boldsymbol{r}' \tag{4a}$$

$$E\left(\boldsymbol{r}\right) = E^{ext}\left(\boldsymbol{r}\right) + \frac{1}{4\pi\epsilon_0}\sum_s \oiint \frac{(\boldsymbol{r}-\boldsymbol{r}')}{|\boldsymbol{r}-\boldsymbol{r}'|^3}\sigma(\boldsymbol{r}')d\boldsymbol{r}' \tag{4b}$$

In (4), $\boldsymbol{r}$ is the position vector of a point over the surface of s, $\emptyset^{ext}(\boldsymbol{r})$ and $E^{ext}(\boldsymbol{r})$ are the potential and field due to external stimulus and $\sigma(\boldsymbol{r}')$ is the surface charge density. The static physics equations are solved at every vertex of the *.msh* file and then combined through the integration in (4) to represent the actual morphological characteristics. The integral is taken over all particle surfaces in the problem and we do not need to apply a bounding sphere as in case of the COMSOL solver [41].

The stem cell surface mesh representations obtained from [23] were not centered around the origin *(0, 0, 0)* in 3D coordinate system. Therefore, we obtained the center of mass of the cell from MeshLab [40], assuming a uniform density for the stem cell, and applied translational operations to re-center the cell at the origin before forwarding the mesh to Scuff-EM for the calculation of the polarizability tensor.

3) NIST Finite Element Method Using Voxel Representation: An open source finite difference and finite element package was developed at NIST to calculate the linear and elastic properties of heterogeneous random materials [43]. The package was developed to be versatile enough for a wide range of applications such as the calculation of the effective properties of random mixtures and composites such as concrete [43]. The package requires the discretization of the object into cubical voxels and therefore was able to operate directly on the voxel representation of the stem cells (see Fig. 2). The accuracy of the package has been validated in a wide variety of applications [44]–[46]. It was used as a third method to crosscheck the polarizability values calculated using the COMSOL and SCUFF-EM packages. This solver will be designated as NIST FEM for the remainder of this paper.

The three solvers discussed in this work employ different numerical recipes for the calculation of the polarizability. For example, Scuff-EM uses a surface mesh because it is based on the integral form of Maxwell's equations whereas COMSOL and the NIST FEM use a volumetric mesh since they employ the differential form of Maxwell's equations [47]. However, if a fine-enough mesh is employed, the three methods should yield the same polarizability values since they are solving identical

TABLE II
SOLVERS USED FOR VARIOUS STEM CELL REPRESENTATIONS

Solver	Voxel	Down1	Down2	Down4	Down8	Down16
NIST FEM	√					
COMSOL FEM				√	√	√
Scuff-EM		√	√	√	√	√

TABLE III
APPROXIMATE COMPUTATIONAL TIME FOR PPS IN HOURS[2]

Solver	Voxel	Down1	Down2	Down4	Down8	Down16
NIST FEM	5.3	N/A	N/A	N/A	N/A	N/A
COMSOL FEM	N/A	N/A	N/A	21	5	0.65
Scuff-EM	N/A	36	2.6	0.08	0.01	2.6×10^{-3}

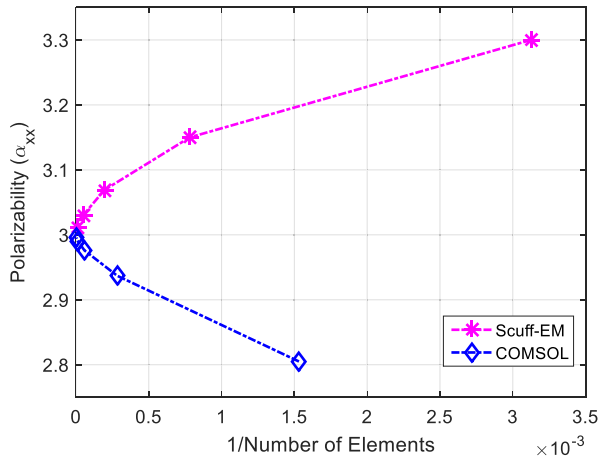

Fig. 4. Depiction of the polarizability convergence between COMSOL and Scuff-EM for a unit sphere. For both solvers, increasing the number of elements will led to the analytical result of 3 [37]. For COMSOL the number of elements = number of 3D tetrahedral elements; for Scuff-EM number of elements = number of faces.

Maxwell's equations for a stem cell with an identical shape and electric properties. The agreement between the three techniques is enforced by the Uniqueness theorem, which states that only one solution can satisfy Maxwell's equations and the boundary conditions of the problem regardless of the numerical technique that is used to achieve this solution [35]. This justifies our approach to compare different solvers to confirm validity of our results. With the variability in the computational domain, the different resolutions of the cell images compatible with corresponding platform is listed in Table II. Beside, we were also concerned about the computational time and resources each simulation occupied which is listed in tabular form for a cell shape (PPS) in Table III.[2]

C. Polarizability Tensors of Simple Cell Shapes

To cross-validate the results of these three techniques, we started by calculating the polarizability tensor of a simple sphere whose polarizability tensor is analytically well-known. Due to its symmetry, a sphere has a diagonal polarizability tensor where the three components are identical and equal to *3* for a sphere with unit volume [34]. Note all the polarizability tensor elements reported in this paper are normalized by particle volume. This simple experiment will help us identify the meshing resolution needed for the accurate calculation of the polarizability tensor of a certain object. Fig. 4 shows the polarizability results versus the inverse of the number of meshing elements used in the calculation (N). As the number of meshing elements increases, the numerical values move towards, with complete agreement in the limit where N^{-1} converges to zero, which is equivalent to an infinite number of meshing elements leading to a continuous object.

[2]All computational times were measured on an Intel Xeon Processor E5-2687W with 20 MB Cache and 3.10 GHz processor base frequency. The values in the table only shows the run time of each solver. An additional $\sim$ 1 hour was needed to adapt the format of each cell to formats that are compatible with each solver.

For Scuff-EM, the number of elements is the number of triangular surface mesh elements and for COMSOL the number of elements is the number of volumetric tetrahedral mesh elements. Linear extrapolation to the $N \rightarrow \infty$ limit facilitates the accurate calculation of the polarizability values using a feasible number of meshing elements. Therefore, in both the COMSOL and Scuff-EM polarizability calculations, the simulations were performed at least two times, with different resolutions, before linear extrapolation was performed to improve the accuracy of the results. To explain the minor differences between COMSOL and Scuff-EM in Fig. 4, it is important to clarify that for both COMSOL and Scuff-EM, the geometry of the stem cell is described by its surface mesh representation. Scuff-EM uses this surface mesh directly to calculate the polarizability tensor. However, COMSOL converts this surface mesh into a volumetric mesh by dividing the medium inside and outside of the surface of the stem cell into volumetric tetrahedrals. Therefore, due to the differences in meshing, small geometrical differences can exist between the COMSOL and Scuff-EM, which can lead to small differences in the calculated polarizability values. However, these differences should diminish as the number of meshing elements is increased as shown in Fig. 4.

D. Electrostatic-Hydrodynamic Analogy

As depicted in Fig. 3(b), the electrical field line around a perfect magnetic conductor is tangential to the surface of the inclusion, which exactly resembles the fluid movement around an insoluble object in a dilute suspension. The fact that electrical field lines around such an inclusion in a dielectric medium is analogous to the fluid movement along a particle in hydrodynamics forms the basis of the Electrostatic-Hydrodynamic analogy [27], [48]. According to this analogy, the intrinsic diffusivity and the intrinsic viscosity of the stem cell can be estimated using the trace of the magnetic and electric polarizability tensors, respectively, as summarized in Table IV [37], [49]. The improvement of the approximation in Table IV

TABLE IV
ELECTROSTATIC-HYDRODYNAMIC ANALOGY

Hydrodynamic properties	Electrostatic properties	Formulae
Intrinsic Viscosity $[\eta]$	Electric polarizability $[\alpha_E]$	$[\eta] \approx \frac{5}{6}[\sigma_\infty] = \frac{5}{6}\frac{tr[\alpha_E]}{3}$
Intrinsic Diffusivity $[D_s]$	Magnetic polarizability $[\alpha_M]$	$[D_s] = [\sigma_0] = \frac{tr[\alpha_M]}{3}$

can be achieved by using the whole polarizability tensor as discussed in [50].

III. RESULTS

A. Validations of the Polarizability Calculations Using Different Solvers

Different solvers require different representations of the cell geometry. For example, NIST FEM requires the volumetric raw voxel representation whereas the Scuff-EM solver requires the STL surface mesh representation. The raw voxel representation of the cell's morphology was converted to a *stereolithography* (STL) surface mesh with varying levels of resolution. The "*down1*" representation has the highest resolution and is closest to the raw *voxel* representation of the cell. The "*down16*" representation has the lowest resolution and the fewest number of surface triangles. Therefore, for an accurate comparison between the NIST FEM results and the Scuff-EM results in Table V, the raw voxel representation was used for the NIST FEM Package whereas the "*down1*" representation was used for Scuff-EM. Even though the "*down1*" surface mesh is close to the volumetric raw voxels, there are still some differences between the two representations. To illustrate these differences, Table VI shows a comparison between the volume of the volumetric raw *voxel* representation and the "*down1*" surface mesh representation of the cells. The percentage variation in the volume between the two representations exceeded 20% for some cell representations. For these cells, the relative differences between the polarizability values calculated using the NIST FEM package and the Scuff-EM solver are comparable to the differences in the volume of the two representations. Table V shows the comparison between the diagonalized electric and magnetic polarizability tensors calculated using the NIST FEM and Scuff-EM solvers. Each family name corresponds to the cell morphology listed in Table I. The polarizability values are dimensionless since they are normalized by the volume of each respective cell. Additional columns in Table V list the relative percent difference between these values as calculated using (5):

$$\%\ \text{Difference} = \frac{|\alpha_{Scuff-EM} - \alpha_{NIST-FEM}|}{\alpha_{Scuff-EM}}\ x\ 100 \quad (5)$$

[3]NIST FEM was performed on the *voxel* representation of each cell morphology.

[4]Scuff-EM was performed on the "*down1*" representation of the surface mesh of each cell.

TABLE V
DIAGONALIZED POLARIZABILITY COMPARISON BETWEEN NIST FEM[3] AND SCUFF-EM[4]

Cell Family	α_E	NIST FEM	Scuff-EM	% diff-erence	α_M	NIST FEM	Scuff-EM	% diff-erence
PPS	P_1	124.16	109.51	13.39	M_1	-2.55	-2.39	6.83
	P_2	19.59	17.86	9.70	M_2	-1.94	-1.85	5.02
	P_3	4.43	4.61	3.86	M_3	-1.38	-1.32	4.75
Collagen Fibrils (CF)	P_1	106.62	105.09	1.46	M_1	-2.80	-2.52	10.90
	P_2	21.67	20.33	6.60	M_2	-1.65	-1.67	1.07
	P_3	1.99	2.44	18.34	M_3	-1.28	-1.31	2.50
Matrigel (MG)	P_1	4.31	4.50	4.14	M_1	-1.82	-1.76	3.28
	P_2	3.99	3.91	2.38	M_2	-1.58	-1.53	3.19
	P_3	3.05	2.94	3.49	M_3	-1.48	-1.43	3.53
Spun-Coat (SC)	P_1	59.09	52.88	11.74	M_1	-5.62	-4.68	20.19
	P_2	13.62	11.73	16.13	M_2	-1.35	-1.38	1.71
	P_3	1.54	1.80	14.38	M_3	-1.17	-1.15	2.09
Nanofiber (NF)	P_1	114.61	113.96	0.57	M_1	-2.81	-2.51	11.70
	P_2	4.17	3.85	8.39	M_2	-1.83	-1.84	0.58
	P_3	2.14	2.50	14.61	M_3	-1.13	-1.15	1.33
SC+OS	P_1	121.97	111.8	9.10	M_1	-3.62	-3.06	18.20
	P_2	31.96	27.43	16.51	M_2	-1.5	-1.55	3.36
	P_3	1.74	2.15	19.07	M_3	-1.24	-1.26	1.68
NF+OS	P_1	92.65	84.06	10.21	M_1	-3.25	-2.91	11.43
	P_2	7.44	6.88	8.14	M_2	-1.7	-1.65	2.71
	P_3	2.41	2.58	6.75	M_3	-1.22	-1.23	0.37
Collagen Gel (CG)	P_1	221.18	192.0	15.20	M_1	-2.8	-2.76	1.37
	P_2	25.38	22.56	12.51	M_2	-1.71	-1.62	5.89
	P_3	10.55	9.24	14.10	M_3	-1.26	-1.05	20.22
Fibrin Gel (FG)	P_1	369.33	299.88	23.16	M_1	-2.25	-2.15	4.51
	P_2	25.68	21.76	18.04	M_2	-1.99	-1.83	8.46
	P_3	8.92	7.93	12.58	M_3	-1.40	-1.19	17.63
Microfiber (MF)	P_1	136.94	129.9	5.42	M_1	-2.27	-2.22	2.47
	P_2	17.34	16.36	5.97	M_2	-1.75	-1.67	5.37
	P_3	5.03	5.09	1.12	M_3	-1.51	-1.44	4.88

We represent the diagonalized electric polarizability values in a descending order such that $P_1 \geq P_2 \geq P_3$. The maximum percentage uncertainty between the NIST FEM and the Scuff-EM results was 23.16% as observed in the case of the electric,α_E, P_1 component of the FG stem cell.

This difference in the P_1 value is justifiable given that the difference in volume between the volumetric raw voxel representation and the surface mesh representation was 21% as shown in Table VI. The diagonalized magnetic polarizability values M_1, M_2, and M_3 are also shown in Table V arranged such

TABLE VI
COMPARISON OF VOLUME OF EACH CELL MEASURED FROM THEIR VOXEL REPRESENTATION AND "DOWN1" SURFACE MESH REPRESENTATION

Cell Family	PPS	CF	MG	SC	NF	SC+OS	NF+OS	CG	FG	MF
Voxel Volume (μm^3)	14960	7128	11965	21162	8315	13074	16247	20157	8036	17880
Mesh Volume ["*down1*"] (μm^3)	17857	8701	13048	27129	9864	17007	19433	24547	10199	20634
% Variation	16.2 %	18.1 %	8.30 %	22.0 %	15.7 %	23.1 %	16.4 %	17.9 %	21.2 %	13.4 %

that $M_1 \geq M_2 \geq M_3$. The maximum difference for the magnetic polarizability values was 20.22% as observed in the P_3 component of the CG cell, which is comparable to the 17.88% difference in the volume of the two different representations used in the NIST FEM and the Scuff-EM packages.

As an additional independent validation step, Table VII compares the polarizability values calculated using the FEM package COMSOL and the Scuff-EM package. In this comparison, the percentage uncertainty is defined as (6):

$$\% \text{ Difference} = \frac{|\alpha_{Scuff-EM} - \alpha_{COMSOL}|}{\alpha_{Scuff-EM}} \, x \, 100 \qquad (6)$$

Both solvers used the "*down*4" representation and, therefore, the agreement was even better and the differences were less than 7% for all of the cell shapes. Note that the difference between Table VII and Table V is that Table V compares the polarizability values calculated by the NIST-FEM solver with the values calculated using the Scuff-EM solver. For Table V, the "*down*1" mesh is used for Scuff-EM and the voxel representation is used for the NIST-FEM solver. Table VII, however, compares the polarizability values calculated using COMSOL with those calculated using Scuff-EM both using the "*down*4" mesh representation of the stem cells. The level of agreement between the three independent solvers summarized in Table V and Table VII adds further validity to the polarizability values reported in this work.

One of the advantages of the NIST stem cell database, not a detriment, is that it provides varying resolution levels for each cell representation. Therefore, we were able to study the effect of the meshing resolution on the calculated values of the polarizability. Scuff-EM was used to calculate the polarizability tensors for all the meshing resolutions, "*down1*" to "*down16*", for the PPS stem cell. Fig. 5(a)–5(c) depict the diagonalized electric polarizability values P_1, P_2, and P_3, respectively, calculated for the PPS stem cell using surface meshes with varying resolutions. Since each mesh has a slightly different volume, the polarizability values were normalized with the volume of each respective mesh. For the case of the PPS stem cell, Fig. 5 shows that if the coarsest representation, "*down16*", is used, the value of P_1 drops by 49.4% from the value calculated using the "*down1*" mesh. Similarly, P_2 and P_3 experienced a decrease of 38.85% and 49.5%, respectively, between "*down1*" and "*down16*". Other stem cells showed the same trend, where the diagonal polarizability components decreased as the mesh resolution became coarser. However, if we consider the ratios P_1/P_2 and P_1/P_3 as depicted in Fig. 5(d) and Fig. 5(e),

TABLE VII
DIAGONALIZED POLARIZABILITY COMPARISON OF "DOWN4" MESH REPRESENTATION BETWEEN SCUFF-EM AND COMSOL

Cell Family	α_E	NIST FEM	Scuff-EM	% diff-erence	α_M	NIST FEM	Scuff-EM	% diff-erence
PPS	P_1	86.426	84.461	2.27	M_1	-2.41	-2.44	0.95
	P_2	14.308	13.677	4.41	M_2	-1.73	-1.74	0.21
	P_3	3.344	3.212	3.93	M_3	-1.22	-1.25	2.16
Collagen Fibrils (CF)	P_1	85.726	80.264	6.37	M_1	-2.75	-2.78	1.2
	P_2	17.078	16.094	5.76	M_2	-1.49	-1.47	1.35
	P_3	1.776	1.703	4.14	M_3	-1.18	-1.17	0.8
Matrigel (MG)	P_1	3.743	3.638	2.81	M_1	-1.67	-1.67	0.14
	P_2	3.474	3.370	2.98	M_2	-1.48	-1.47	0.61
	P_3	2.766	2.680	3.11	M_3	-1.43	-1.42	0.32
Spun-Coat (SC)	P_1	47.097	46.065	2.19	M_1	-4.78	-4.86	1.73
	P_2	10.815	10.504	2.88	M_2	-1.27	-1.26	0.83
	P_3	1.459	1.426	2.26	M_3	-1.09	-1.10	0.69
Nanofiber (NF)	P_1	95.572	89.274	6.59	M_1	-2.63	-2.68	1.8
	P_2	3.679	3.538	3.85	M_2	-1.66	-1.64	1
	P_3	1.891	1.822	3.68	M_3	-1.10	-1.07	2.29
SC+OS	P_1	94.722	92.292	2.57	M_1	-3.26	-3.27	0.41
	P_2	23.793	23.635	0.66	M_2	-1.41	-1.36	3.33
	P_3	1.617	1.603	0.85	M_3	-1.18	-1.19	0.97
NF+OS	P_1	69.285	67.121	3.12	M_1	-3.00	-3.03	1.19
	P_2	5.718	5.515	3.56	M_2	-1.53	-1.49	2.21
	P_3	1.919	1.857	3.24	M_3	-1.15	-1.09	5.21
Collagen Gel (CG)	P_1	131.27	125.19	4.63	M_1	-2.31	-2.30	0.49
	P_2	15.595	15.164	2.76	M_2	-1.79	-1.77	0.99
	P_3	7.037	6.791	3.48	M_3	-1.14	-1.07	6.34
Fibrin Gel (FG)	P_1	212.89	206.42	3.04	M_1	-1.94	-2.02	3.94
	P_2	15.923	15.385	3.38	M_2	-1.75	-1.82	4.23
	P_3	5.846	5.618	3.9	M_3	-1.19	-1.24	4.68
Microfiber (MF)	P_1	99.210	92.633	6.63	M_1	-2.00	-1.99	0.26
	P_2	12.893	12.208	5.31	M_2	-1.74	-1.76	1.29
	P_3	3.898	3.739	4.08	M_3	-1.33	-1.38	3.44

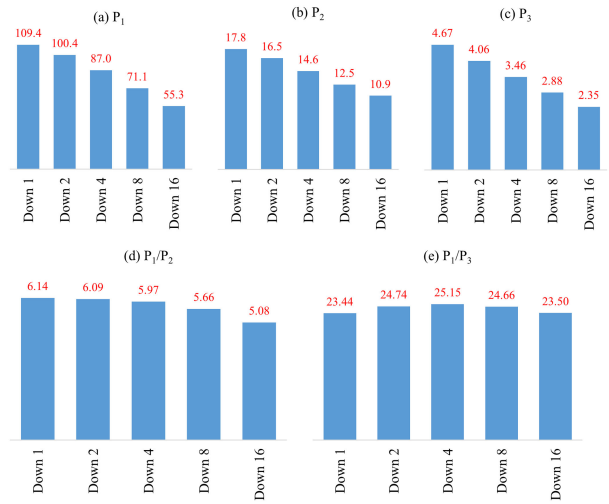

Fig. 5. Histogram of diagonalized electric polarizability tensor of the PPS cell (for the specific cell identifier mentioned in Table I); (a) showing 49.4% decrease in the P_1 value, (b) 38.9% decrease in P_2 value and (c) showing 49.5% decrease in the P_3 value as the resolution is decreased from "*down*1" to "*down*16". The individual values of P_1, P_2, P_3 are sensitive to the meshing resolution while their ratios P_1/P_2 and P_1/P_3 are much less sensitive. The polarizability values are dimensionless since they are normalized by the volume of respective cell.

respectively, a much smaller change in the ratios is exhibited as the meshing resolution becomes coarser. The results in Fig. 5 were achieved using the PPS stem cell but several other cell shapes showed a similar behavior but they were not included in Fig. 5 for conciseness. Therefore, we can conclude that the absolute polarizability values vary significantly with the resolution of the mesh, but the polarizability ratios are less sensitive to the meshing resolution. Therefore, if accurate absolute values for the polarizabilities are required, the highest resolution should be used in the calculation. However, if only the ratios of the main polarizability components are required, a coarse meshing representation can provide a good estimate at significant savings in the computational time.

B. Elements of the Electric Polarizability Tensor

Another goal of this paper was to investigate different ways to visualize any correlations between the polarizability results and the shapes of the different stem cells. The diagonal elements of the electric polarizability tensor are always represented in descending order ($P_1 \geq P_2 \geq P_3$). A spherical cell would have $P_1 = P_2 = P_3$ due to its symmetry, with $\frac{P_1}{P_2} = \frac{P_1}{P_3} = 1$. The closer a stem cell is to being spherical, the closer its polarizability ratios P_1/P_2 and P_1/P_3 will be to unity. Similarly, a 2D circular disk would have $P_1 = P_2$ and both components will be significantly larger than the third component P_3 [48]. A 1D rod would have P_1 significantly larger than the other two components, P_2 and P_3, and if the rod has a circular cross section then $P_2 = P_3$. Therefore, a 2D plot having these two polarizability ratios as axes would effectively represent the shape and electrical behavior of any 3D object. Fig. 6 captures the effective dimensionality of the 10 different cell morphologies considered. The bottom left corner electrically represents a spherical cell having

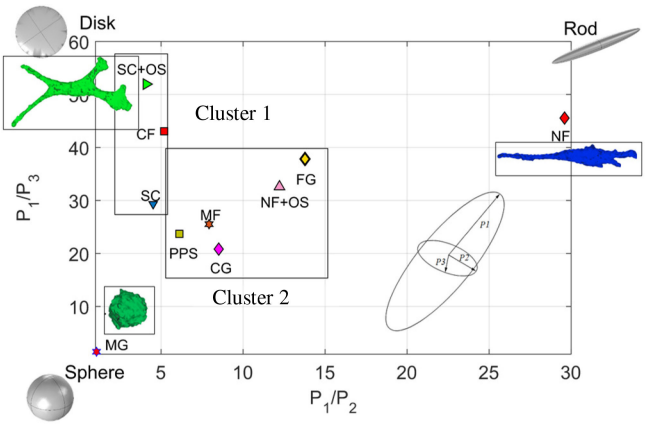

Fig. 6. Encoding shape information from α_E. The polarizability values are ordered such that $P_1 \geq P_2 \geq P_3$. When P_1/P_2 and P_1/P_3 are plotted, the upper right corner represents 1D rod-like shape, top left corner is more 2D disk-like shapes and the bottom left corner is more 3D sphere-like. Cluster 1 represents the cell families grown on a planar substrate hence obtaining a 2D disk like morphology while cluster 2 represents the cell families grown on 3D scaffolds.

$\frac{P_1}{P_2} = \frac{P_1}{P_3} = 1$; likewise, the top left corner represents a 2D disk since $\frac{P_1}{P_2} = 1$ and $\frac{P_1}{P_3} \to \infty$ and top right corner represents a 1D rod having $\frac{P_1}{P_2} = \frac{P_1}{P_3} \to \infty$.

Cells cultured on planar substrates (SC+OS, CF, SC) were closest to the top left corner of the plot, electrically representing a 2D disk like behavior. Among the cells grown in 3D scaffolds (NF, NF+OS, MF, PPS, MG, FG, CG), MG-grown cells are closest to being spherical, indicating equi-axial morphology. The remaining substrate groups showed elongated morphologies with NF being closest to the 1D rod corner. Therefore, the polarizability ratios can be considered as alternative morphology specifiers, given that the diagonalized polarizability values are arranged in descending order ($P_1 \geq P_2 \geq P_3$), which is equivalent to aligning the cell such that its major axis is parallel to the *x-axis*. The data in Fig. 6 were achieved using only 1 morphology per cell family as detailed in Table I, and therefore the previous observations will be re-checked for a larger number of cells in the following sections.

Another visualization technique to present the data summarized in the three diagonalized components of the polarizability matrix can be performed by calculating the polarizability of the cell at different orientations. Rotating the cell along any of the axes will effectively alter the polarizability matrix since by rotating the cell we are altering the dimension and distribution of the original cell morphology. The resulting polarizability matrix after re-orienting the cell, ***A'***, can be obtained by applying (7),

$$A' = RAR^T \tag{7}$$

where ***A*** is the original polarizability matrix, ***R*** is the matrix for proper rotations and $\boldsymbol{R^T}$ is the transpose of ***R***. For simplicity, let us assume P_1 is parallel to the *x-axis*, P_2 is parallel to the *y-axis,* and P_3 is parallel to the *z-axis* in the Cartesian coordinate system. If the cell is rotated around the *y-axis*, the rotation matrix can be designated as R_y and if the cell is rotated around the *z-axis* the rotation matrix can be designated as R_z. If the cell

is rotated around both the *y-axis* and the *z-axis*, the effective rotation matrix can be expressed as (8):

$$R = R_y R_z = \begin{bmatrix} \cos\beta & 0 & \sin\beta \\ 0 & 1 & 0 \\ -\sin\beta & 0 & \cos\beta \end{bmatrix} \begin{bmatrix} \cos\gamma & -\sin\gamma & 0 \\ \sin\gamma & \cos\gamma & 0 \\ 0 & 0 & 1 \end{bmatrix}$$
$$= \begin{bmatrix} \cos\beta\cos\gamma & -\cos\beta\sin\gamma & \sin\beta \\ \sin\gamma & \cos\gamma & 0 \\ -\sin\beta\cos\gamma & \sin\beta\sin\gamma & \cos\beta \end{bmatrix} \quad (8)$$

where β = the angle of rotation around the *y-axis* and γ = the angle of rotation around the *z-axis.* The effective polarizability tensor ***A'*** can now be expressed as (9):

$$A' = \begin{bmatrix} \cos\beta\cos\gamma & -\cos\beta\sin\gamma & \sin\beta \\ \sin\gamma & \cos\gamma & 0 \\ -\sin\beta\cos\gamma & \sin\beta\sin\gamma & \cos\beta \end{bmatrix} \mathrm{X} \begin{bmatrix} P_1 & 0 & 0 \\ 0 & P_2 & 0 \\ 0 & 0 & P_3 \end{bmatrix}$$
$$\mathrm{X} \begin{bmatrix} \cos\beta\cos\gamma & \sin\gamma & -\sin\beta\cos\gamma \\ -\cos\beta\sin\gamma & \cos\gamma & \sin\beta\sin\gamma \\ \sin\beta & 0 & \cos\beta \end{bmatrix} \quad (9)$$

If we focus on only the *xx* component of the resultant polarizability matrix, it can be expressed as (10):

$$\alpha_{E_{xx}} = P_1\cos^2\beta\cos^2\gamma + P_2\cos^2\beta\sin^2\gamma + P_3\sin^2\beta \quad (10)$$

For a spherical cell, since $P_1 = P_2 = P_3 = 3$, $\alpha_{E_{xx}}$ will always have a constant value of three. For the case of an oblate ellipsoid or a 2D disk, $P_1 = P_2$, and therefore the resultant $\alpha_{E_{xx}} = P_1\cos^2\beta + P_3\sin^2\beta$ will only vary with respect to β (rotation along *y-axis*). Equation (10) cannot be simplified further in case of a prolate ellipsoid or 1D rod like morphology since $P_1 >> P_2$ and $P_1 >> P_3$ implying that $\alpha_{E_{xx}}$ will vary for both β (rotation along *y-axis*) and γ (rotation along *z-axis*) for a 1D rod-like morphology. These observations can be used to interpret polarizability measurements from a single cell at multiple orientations to identify whether the cell is more spherical, more oblate-like, or more prolate-like in shape.

To clarify these observations, Fig. 7 shows a plot of $\alpha_{E_{xx}}$ from (10) for different cell types. In each subplot, the $\alpha_{E_{xx}}$ value is normalized by P_1 for different combination of β and γ values. Fig. 7(a) shows the case of a sphere and it is clear that the rotations around the *y-axis* or *z-axis* will have no impact on the value of $\alpha_{E_{xx}}$. Fig. 7(b) shows the "*stripes*" pattern typical of a 2D disk where the $\alpha_{E_{xx}}$ values will change with respect to rotation angles around the *y-axis* but will stay constant with rotations around the *z-axis*. This is why Fig. 7(b) is constant for different values of γ and varies with β. For a 1D prolate shape, the values of $\alpha_{E_{xx}}$ will vary with β and γ creating the rounded-square pattern shown in Fig. 7(c). Fig. 7(d) shows the value of $\alpha_{E_{xx}}$ due to the variations in β and γ, according to (10), for the Matrigel cell shape. By comparing Fig. 7(d) with Fig. 7(a), the polarizability values of Matrigel at multiple cell orientations can be used to infer its approximately spherical shape. In the case of the SC+OS cell, it has a flattened morphology with multiple rod-like protrusions and, therefore, we expect the polarizability behavior for multiple orientations to provide a pattern that is a hybrid of the oblate and prolate patterns. Fig. 7(e) shows the $\alpha_{E_{xx}}$ due to the variations in β and γ for the SC+OS cell and it is clear that the pattern is a hybrid of the pattern in Fig. 7(b) and that in Fig. 7(c). The NF cell shape is very close to that of a prolate ellipsoid and therefore its $\alpha_{E_{xx}}$ pattern in Fig. 7(f) shows significant resemblance to that of a 1D prolate rod shown in Fig. 7(d).

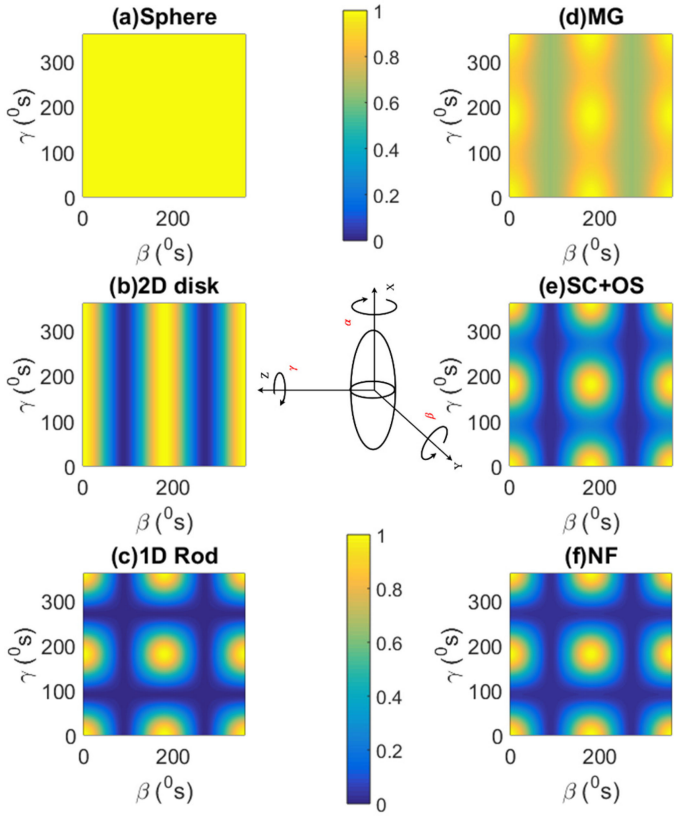

Fig. 7. Pseudo-color (checkerboard) plot of $\alpha_{E_{xx}}$ normalized by P_1 (adjacent color bar showing the values of $\alpha_{E_{xx}}$ normalized to the maximum value found). β is the angle of rotation around the *y-axis* and γ is the angle of rotation around the *z-axis* (in degrees). For each subplot, only one cell is shown from each family. The "*022614_SJF_Matrigel_1d_63x_05*" cell from the MG family (d) is similar to a sphere (a). The "*080713_SJF_NF1_d1_63x_18*" cell from the NF family (f) electrically resembles a 1D rod shown in (c). The "*091313_SJF_SC+OS_d1_ 63x_18*" from the SC+OS family (e) does not accurately replicate the behavior of a 2D disk (b) because of its distribution along minor semi-axis.

It is important to emphasize that the previously described observations were achieved using only a single morphology from each cell family. Within each family, there is significant cell-to-cell variability and, therefore, a larger number of cells from each family needs to be examined before these observations can be converted into solid conclusions. However, the main contribution of this Section is to: (*i*) adapt multiple numerical techniques to accurately calculate the polarizabilities of highly complex stem cells, (*ii*) quantify how the polarizabilities depend on the resolution of the mesh used to represent the stem cell, and (*iii*) develop efficient techniques to visualize the variations in theses polarizabilities between different cells within the same family or in different families.

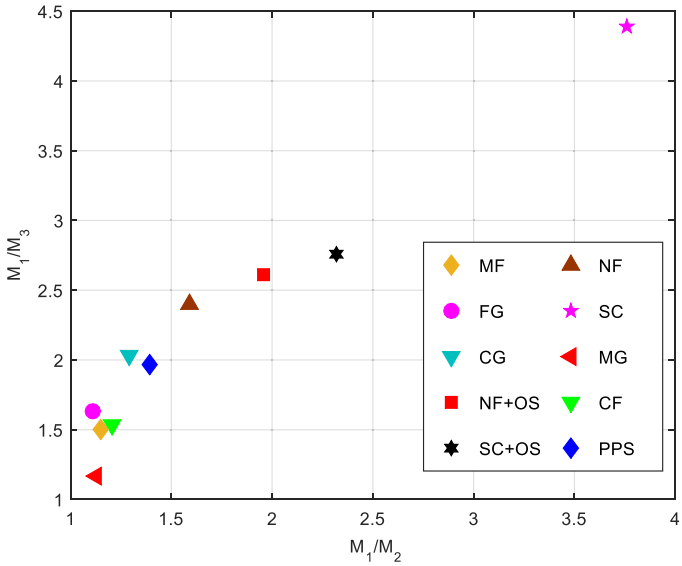

Fig. 8. Encoding shape information from α_M. The ratios are plotted in the same manner as Fig. 6. However, the range of ratio values is not as expansive as in Fig. 6, which was calculated from α_E. The coordinates for SC+OS and SC, which had the most flat morphology, are located at the top right corner indicating that the principle polarizability value is larger than the other two polarizability values, as in a 2D disk-like morphology. Only one morphology is used for each cell family as described in Table I.

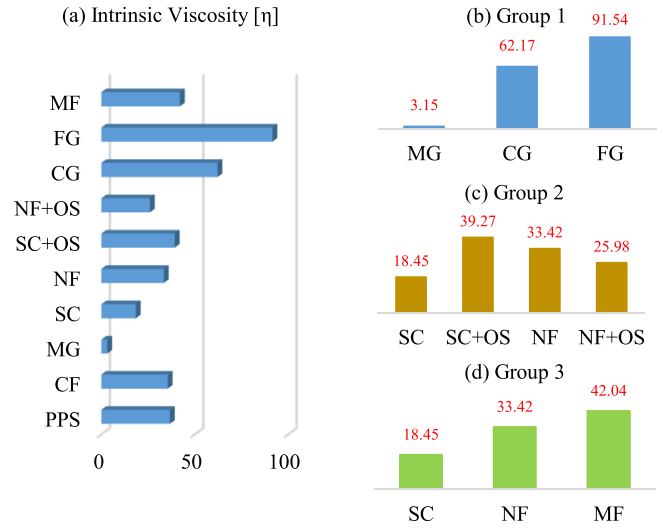

Fig. 9. (a) Histogram plot of the intrinsic viscosity $[\eta]$ of ten cell shapes. (b) Group 1 had the same building material (hydrogel) yet show a difference in $[\eta]$, (c) Group 2 indicates addition of a soluble factor (OS) might increase the value of $[\eta]$ in planar substrates (d) Group 3 is based on the 3 families made from same polymer [poly(ε- caprolactone), PCL].

C. Elements of the Magnetic Polarizability Tensor

We also calculated the magnetic polarizability tensor (α_M) values, M_1, M_2, and M_3, and plotted the values for the 10 different cell shapes in Fig. 8. The diagonalized magnetic polarizability values were arranged in descending order $M_1 \geq M_2 \geq M_3$. Similar to Fig. 6, the *x-axis* of Fig. 8 shows the ratio M_1/M_2 and the *y-axis* shows the ratio M_1/M_3. Comparing Fig. 8 with Fig. 6, it is clear that the magnetic polarizability values are concentrated within a smaller range than the electric polarizability values. Hence, the α_M values are more challenging to use as a shape classifier than the α_E values. Even so, some observations can be derived from Fig. 8. Magnetic polarizability components show an opposite trend to that of the electric polarizability components discussed in the previous section. Hence, disk-like oblate ellipsoids will have an M_1 value that is significantly larger than the M_2 and M_3 components [48]. Therefore, any object having a flat morphology, similar to that of a thin oblate ellipsoid, will have an M_1 value that is significantly larger than the M_2 and M_3. Consequently, the upper right corner of Fig. 8 will represent a disk-like shape. That is why we observed the largest values of M_1/M_2 and M_1/M_3 for the SC and SC+OS stem cells, implying the same observation we drew from Fig. 6 that cells cultured on a 2D substrate are more likely to behave as a 2D disk under an external electrical field. Similar to the previous subsection, the observations achieved from Fig. 8 were obtained using a single shape from each family and a larger number of cells from each family will be simulated in the future to draw more accurate conclusions.

D. Intrinsic Viscosity

By using the Electrostatic-Hydrodynamics analogy, we can use the electric polarizability values to calculate the intrinsic viscosity of the stem cells. This will allow us also to quantify how the cell's morphology impacts the intrinsic viscosity η of the cell (see Table IV), a quantity that describes the presence of the cells at low concentration increases the viscosity of the fluid overall. Intrinsic viscosity is a measure of the contribution of the suspended particles to the overall suspension viscosity. It is defined as $[\eta] = \lim_{\phi \to 0} \frac{\eta - \eta_0}{\phi \eta_0}$, where $[\eta]$ is the intrinsic viscosity of the suspended particles, ϕ is the volume fraction of the suspended particles, η_0 is the viscosity of the solution in absence of the suspended particles, and η is the viscosity of the suspension. We can calculate the intrinsic viscosity, using the analogy in Table IV, from the polarizability results.

Fig. 9 shows the intrinsic viscosity of the 10 different stem cells. MG, FG and CG are all obtained from hydrogel yet their $[\eta]$ values differ significantly. CG and FG have significantly large $[\eta]$ compared to other cell morphologies because of their distributed volume. The NF and the NF+OS cells were grown in a geometrically identical environment but with different chemical composition since the soluble factor Osteogenic Supplements (OS) was added only to the NF+OS cells. The comparison of the $[\eta]$ of the NF and the NF+OS cells, and the $[\eta]$ of the SC and the SC+OS cells, indicates that modifying the chemical composition of a cell's environment can affect its intrinsic viscosity $[\eta]$.

E. Intrinsic Conductivity $[\sigma]$ for Variable Conductivity Contrast Δ

So far, we have only considered the calculation of the electric and magnetic polarizability tensors α_E and α_M. The α_E values

are calculated when the ratio between the electrical conductivity of the cell and the electrical conductivity of its environment is equal to infinity, whereas the α_M values are calculated when this ratio is equal to zero. Therefore, α_E and α_M represent the two limiting cases for the electrostatic polarizability. In a practical scenario, the cell will have a finite contrast with respect to its environment. The ratio between the electrical conductivity of the cell and the electrical conductivity of its environment, Δ, will be finite and non-zero. Garboczi and Douglas introduced a Padé approximant formulation that we use to estimate the intrinsic conductivity of a particle, $[\sigma]_\Delta$, with an arbitrary shape at finite contrast via the knowledge of only $[\sigma]_0$ and $[\sigma]_\infty$, where these quantities are defined as $[\sigma]_\infty = \frac{1}{3}tr(\alpha_E)$ and $[\sigma]_0 = \frac{1}{3}tr(\alpha_M)$ [44]. The intrinsic conductivity $[\sigma]_\Delta$ represents the average polarizability of the particle at multiple orientations when the particle has an arbitrary contrast Δ with respect to its environment. Similarly, $[\sigma]_0$ and $[\sigma]_\infty$ represent the average polarizability of the particle at multiple orientations for $\Delta = 0$ and $\Delta = \infty$, respectively. Equation (11) gives the Padé approximant as [44]:

$$[\sigma]_\Delta = \frac{[\sigma]_\infty (\Delta - 1)^2 + a\ (\Delta - 1)}{(\Delta - 1)^2 + \left([\sigma]_\infty + \frac{a}{d}\right)(\Delta - 1) + a} \tag{11}$$

where $d =$ spatial dimensionality of the particle. For our study, all particles are 3D (even the flattened cells). The parameter a is a shape dependent parameter defined as follows [44]:

$$a = \frac{[\sigma]_\infty - [\sigma]_0 + [\sigma]_\infty [\sigma]_0}{1 + \left(1 - \frac{1}{d}\right)[\sigma]_0} \tag{12}$$

The accuracy of the Padé approximant was demonstrated for a wide variety of shapes such as worm-like carbon nanotubes and crumpled graphene flakes [37]. In this work, our goal was to test the accuracy of the Padé approximant for shapes as complicated as the stem cell morphologies shown in Fig. 1. The Padé approximant can significantly reduce the computational time needed for numerical computation of $[\sigma]_\Delta$. Fig. 10(a) and Fig. 10(b) show the Padé approximant versus the intrinsic conductivity calculated using COMSOL for the PPS and FG stem cells, respectively, at "*down4*". As shown in Fig. 10, the good agreement between the Padé approximant and the COMSOL calculations for multiple contrast values, Δ, validate the approximation. Using COMSOL, the intrinsic conductivity at each Δ value required ~ 21 hours of run time whereas the Padé approximant required essentially no time at all, provided that $[\sigma]_0$ and $[\sigma]_\infty$ were calculated beforehand.

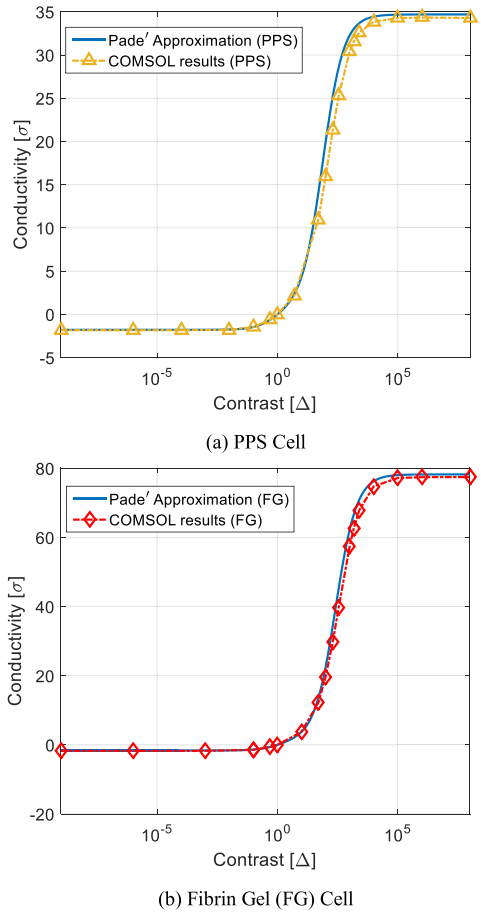

Fig. 10. Padé approximation for the intrinsic conductivity values in comparison to the COMSOL results obtained for 20 different finite contrasts (Δ) illustrated for the case of two families (a) PPS and (b) FG. Each of the FEM simulations took approximately 1 day whereas the Padé approximation can approximate the same in seconds if only the $[\sigma]_0$ and $[\sigma]_\infty$ values are provided.

F. Minimum Enclosing Ellipse (MEE)

So far, all our previous results only considered 10 cell morphologies, one from each family. Our goal now is to explore the variations in the polarizability of cells with respect to different cells within each family. Therefore, we calculated the electric polarizability values, i.e., $\Delta = \infty$, of hundreds of shapes from each of the ten families to observe the variance in the calculated values. Since the Padé approximant only estimates the polarizability values at a finite contrast Δ and given that the three different solvers used in this work showed excellent agreement, only the Scuff-EM solver was used for all the cell shapes because of its' reduced computational time requirement. In each case, the "*down4*" representation of each cell was used. The "*down4*" representation is not the finest mesh but if we focus on the polarizability ratios, $\frac{P_1}{P_2}$ and $\frac{P_1}{P_3}$, similar values can be achieved as those achieved using the "*down1*" representation with the highest resolution as concluded from Fig. 5. This section summarizes the results of hundreds of stem cell polarizability ratios from the ten different families. One powerful tool to extract the useful observations from this large set of results is to enclose the polarizability ratios, $\frac{P_1}{P_2}$ and $\frac{P_1}{P_3}$, obtained from the hundreds of morphologies simulated from each family into a hyper-sphere (in this case a 2D ellipse) [51].

The dimension of the hyper-sphere will then contain the information about the variance of the data set. Khachiyan *et al.* first introduced the algorithm as an optimization problem to find the ellipsoid with the smallest volume that encloses all the given data points in an n-dimensional space in [51]. The general form of an ellipsoid in center form can be written as (13) [52]:

$$\varepsilon = \{x \in \mathbb{R}^n | (x\ -\ c)^T A\,(x\ -\ c) = 1\} \tag{13}$$

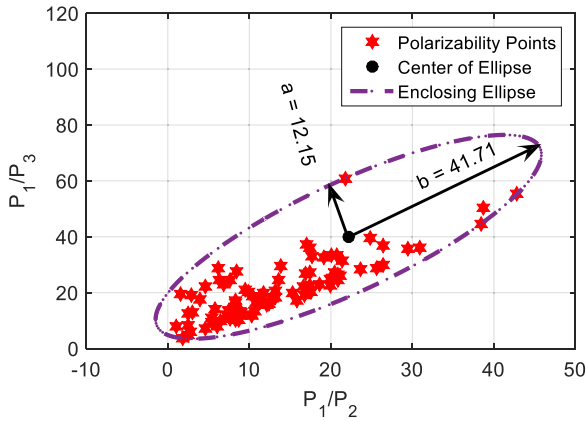

Fig. 11. Implementation of Minimum Enclosing Ellipse (MEE) to represent the 87 polarizability ratios calculated from 87 different cell morphologies from the MF family. The parameters *a* and *b* are the lengths of the semi-axes of the ellipse.

TABLE VIII
THE SEMI-AXES OF THE MINIMUM ENCLOSING ELLIPSE (MEE) ALGORITHM FOR ALL TEN CELL FAMILIES

Family	Number of Cells	*a*	*b*	Area	Tilt Angle (°)
MF	87	12.2	41.7	1592.09	59.47
NF	101	35.1	63	6937.76	61.02
NF+OS	95	27.8	73.8	6443.37	62.79
CF	102	34.6	99.9	10870.5	82.56
SC	99	29.6	69.5	6452.29	80.78
SC+OS	96	26.2	79.3	6536.3	78.24
CG	101	30.3	93.2	8878.54	76.41
FG	92	14.8	48.5	2262.06	71.37
PPS	98	13.4	40.2	1686.84	87.84
MG	98	1.14	9.39	33.63	64.17

where x are the data points, c is center of the ellipsoid in n dimensional space and A is an $n \times n$ matrix containing the information about dimension and orientation of the ellipsoid. The volume of the ellipsoid in this form is given by (14) [52]:

$$Vol\,(\varepsilon) = \frac{\nu_o}{\sqrt{\det\,(A)}} = \nu_0 \det\left(A^{-1}\right)^{\frac{1}{2}} \tag{14}$$

where ν_0 is the volume of the unit hypersphere in dimension n. Now, to enclose a set of m data points in n dimensional space $S = \{f_1, f_2, f_3, \ldots f_m\} \in \mathbb{R}^n$, we must impose the constraints that all the m points f_i are inside the boundary of the ellipsoid [52] i.e.,

$$(f_i - c)^T A\,(f_i - c) \leq 1 \qquad i = 1, 2 \ldots m \tag{15}$$

So, the optimization problem can be formulated as (16)

$$\begin{aligned} &minimize \quad \det\left(A^{-1}\right) \\ &subject\ \ to \quad (f_i - c)^T A\,(f_i - c) \leq 1 \qquad i = 1, 2 \ldots m \end{aligned} \tag{16}$$

Calculating the *singular value decomposition (SVD)* of matrix A will provide us the information about the length of the semi-axes and orientation of the principal axes of the enclosing ellipse [52]. Adopting the numerical implementation of the above-mentioned algorithm, we simulated all cell morphologies in the NIST database. The electric polarizability ratios from each of the ten families are then clustered as a minimum area ellipse as shown in Fig. 11. The successful implementation of MEE is demonstrated for the case of one cell family (e.g., Microfibers (MF)) in Fig. 11. We opted for calculating the MEE that encloses all the polarizability values even the outliers as shown in Fig. 11. We could have focused on obtaining a smaller MEE by enclosing a smaller percentage of the cells (∼80% for example) that show similar polarizability values. But we opted for calculating the MEE as indication of the maximum variability in the polarizability values that can be obtained in each family.

We computed the enclosing ellipse for all the ten cell families in similar fashion. Table VIII summarizes the number of cells simulated from each family as well as the properties of the MEE such as the semi-minor axis (a), the semi-major axis (b), the area of the MEE, and the tilt angle the MEE makes with the *x-axis*. Since $P_1 \geq P_2 \geq P_3$, the minimum tilt angle is 45° which occurs when occurs when $P_2 = P_3$. Large tilt angles, indicate that the ratio between P_1/P_3 and P_1/P_2 is large (i.e., $\frac{P_1}{P_3} \gg \frac{P_1}{P_2}$), indicating that P_2 is significantly larger than P_3. Therefore, large tilt angles indicate shapes which have two dimensions larger than the third, i.e., oblate in nature, whereas small tilt angles indicate shapes that have one dimension larger than the other two, i.e., prolate in nature.

To make the observation visually less complicated, we divided the MEE of the 10 cell families into three different subplots in Fig. 12. The subplots were categorized according to the scaffold material and characteristics of the cell families. MF, NF, and NF+OS are grouped in one subplot, Fig. 12(a), since they all were made from the same PCL polymer. Fig. 12(b) incorporates the three cell families that were grown on 2D planar scaffolds CF, SC, and SC+OS. The remaining scaffolds CG, FG, and MG are 3D scaffolds, and their MEE polarizability results are grouped together in Fig. 12(c).

From the cell clustering, we can deduce some significant understanding about the electrical behavior of the ten different cell families. The MEE for the MF family has the smallest area of the three cell families in Fig. 12(a), indicating less variations in the cell's polarizability values than the NF and the NF+OS families. For the MF family, the cells were grown on a scaffold composed of microfibers whereas for the NF family the cells were grown on a scaffold composed of nanofibers. Therefore, the main conclusion from Fig. 12(a) is that the larger features sizes of the MF scaffold reduce the possible shape variations similar to the case of a pixelated screen where coarser resolutions lead to fewer pixels per unit area and a smaller number of possible shape variations.

The results in Fig. 12(a) and Fig. 12(b) show that adding a soluble factor (i.e., Osteogenic Supplement) to create the SC+OS and NF+OS scaffolds, generate cells with polarizability values that cover the same range of values as the SC and NF cells. The same conclusion can be achieved from Table VIII which shows that the MEE area and tilt angle of the SC family and the

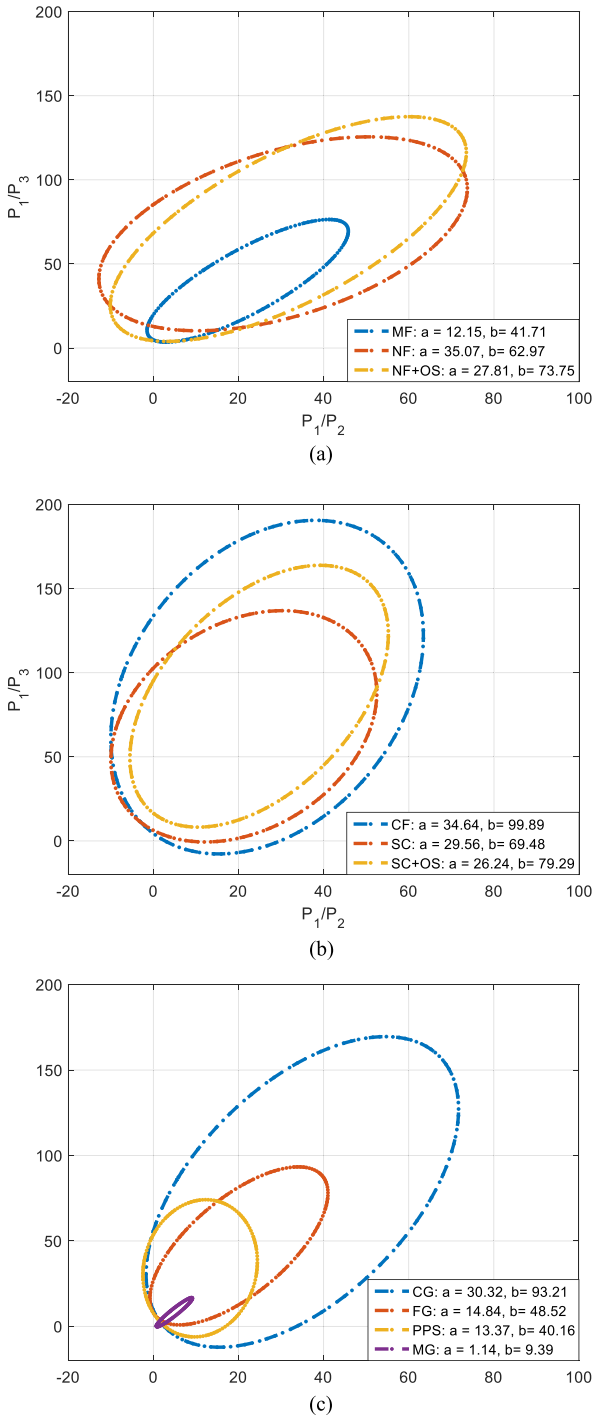

Fig. 12. Cluster presentation of (a) NF, MF, NF+OS; (b) CF, SC, SC+OS and (c) CG, FG, PPS, MG using Minimum Enclosing Ellipse (MEE). (results obtained from Scuff-EM using the "*down*4" mesh representation). *a* is the semi minor-axis and *b* is the semi major-axis of respective minimum area ellipse for each cell family.

SC+OS are very similar. Similar observations can be achieved by comparing the NF and the NF+OS values in Table VIII.

The cell family showing the most variations, that is the MEE with the largest area, is the CF family. The scaffold used for this family is 2D in nature and Fig. 12(b) shows that 2D scaffolds (SC, SC+OS, and CF) typically lead to more variations in the polarizability values of cells than most 3D scaffolds. The SC, SC+OS, and CF families also show higher tilt angles than most other families. This can be seen by comparing the orientations of the MEEs in Fig. 12(a) and Fig. 12(b) and also by looking at the tilt angle entries in Table VIII. Therefore, the SC, SC+OS, and CF families lead to cells which are more oblate in shape than the other families.

The remaining 3D families in Fig. 12(c) show that the CG family has the largest variations followed by the FG, then the PPS family, and the MG gamily shows the least variations. This can be observed by comparing the areas of the ellipses in Fig. 12(c) and the entries in Table VIII. The MG scaffold generate cells which are almost spherical in shape with minimal variations and therefore their polarizability values are clustered over the smallest areas.

A final comment on the Fig. 12 and Table VIII is that these results were obtained from a finite number of cells. Larger cell distributions are needed to draw firm conclusions about the cell populations grown under different conditions. However, the current paper focuses on the methodology of calculating the polarizability values for complex shaped cells and how to visualize their variations in a clear and informative manner.

IV. Discussions

The numerical experiments performed in this work validate the calculated polarizability values and shed light on the advantages and disadvantages of different numerical techniques and meshing resolution. However, more importantly, calculating the polarizability tensors at any contrast between the cell and its environment paves the way to many applications such as predicting the hydrodynamic, dielectrophoresis, and electroporation response of stem cells. For example, by invoking the well-established theory of the Electrostatic-Hydrodynamic analogy [27], we can predict the variations in the hydrodynamic properties of stem cells grown in different environments. Dielectrophoresis (DEP), defined as the force exerted on a cell due to a specific electrical excitation, is directly proportional to the elements of the generalized polarizability tensor [53]. This force, $\overrightarrow{F_{DEP}}$, acting on a cell can be quantified as (17) [53]

$$\overrightarrow{F_{DEP}} = \frac{1}{2}\alpha V \left(\nabla E^2\right) \tag{17}$$

where, α is the volume normalized polarizability of the particle, V is the volume of the cell. Therefore, the DEP force has a strong dependency on the polarizability of the cell or particle in general [54]. The DEP force has been frequently employed in the separation of particles with different shapes and properties. This is because, particles with different shapes will have different polarizability values, α, leading to different forces that can be leveraged in separating a heterogeneous mixture of particles. Frederick *et al.* successfully employed this phenomena to isolate cancer cell line MDA231 from *erythrocyte* and *T lymphocyte* blood cells in an *in vitro* condition [54]. They observed that, cancer cell lines experience a different DEP force than the normal cells when subjected to a rotating electric field due to their variation in morphology, microvilli inclusion and membrane folds.

Regtmeier *et al.* experimentally evaluated the differences in polarizability between two DNA fragments of different shapes: *(i)* linear and (*ii*) supercoiled. Based on this differences in polarizability, the DNA fragments with different shapes experienced different $\overrightarrow{F_{DEP}}$ behavior which was successfully leveraged for their separation [55]. The main goal of this work is to explore different computational techniques to calculate the polarizabilities of realistic and complex cell shapes grown in different environments. Accurate calculation of these polarizability values can help in predicting the $\overrightarrow{F_{DEP}}$, experienced experimentally by cells, guiding cell separation experiments similar to those reported in [56]–[59].

The induced transmembrane voltage (ITV) on the cell membrane under the excitation of an external electric field is also a direct function of the polarizability of the cell and its electric properties [60]. The ITV plays a significant role in the formation of aqueous pores, termed electroporation, which emerge at the cell membrane locations where the ITV exceeds a certain threshold [61]. This enables the introduction of therapeutic drugs into the cell, which are not easily passed through the membrane in natural conditions [61]. Therefore, an accurate calculation of the polarizability of a stem cell will shed light on the effectiveness of the electroporation process due to a specific electric stimulus.

On a different note, there is significant interest in the overall electrical properties of tissues made of a composite of cells and other structures. By invoking the Effective Medium Approximation, the effective electrical properties of these tissue can be expressed as a function of the polarizability of the constituting cell types [62]. Therefore, the calculation of the polarizability of cells of different shapes can be used to predict the effective electric properties of tissues [62].

V. Conclusions

In this paper, the electric properties of a large number of stem cells with realistic three-dimensional (3D) morphologies are calculated. The stem cell morphologies were obtained from a database recently introduced by the National Institute of Standards and Technology. The electric properties that we focused on were the electrostatic electric polarizability, the magnetic polarizability, and the polarizability at an arbitrary contrast. Multiple computational techniques and multiple resolutions were tested for each cell for cross-validation and to show the effect of shape resolution on the electrical polarizabilities. This work shows that the environment of the stem cells can have a significant effect on the shape leading to polarizability values that are significantly different from each other and from a simple sphere. Furthermore, we introduced different techniques to visualize the variations in the polarizability values with respect to the shape of different cells from within one family and with respect to cells from different families. Finally, a Padé approximant was shown to accurately estimate the polarizability of a stem cell at arbitrary electrical conductivity contrast using only the electric and magnetic polarizabilities. We believe that these results can be used as a benchmark for the polarizability calculation of 3D biological and non-biological particles with complex 3D shapes. Moreover, in many previously reported studies, the shape of stem cells were assumed to be approximately spherical when designing experiments for their electric characterization and during the interpretation of the measured results. The polarizability values in this work will aid in designing more accurate experiments and a more accurate interpretation of the measurement results, which has the potential to advance the electrical characterization of biological cells.

References

[1] P. Rangamani *et al.*, "Decoding information in cell shape," *Cell*, vol. 154, no. 6, pp. 1356–1369, 2013.

[2] S. W. Chan *et al.*, "An expert system for the detection of cervical cancer cells using knowledge-based image analyzer," *Artif. Intell. Med.*, vol. 8, no. 1, pp. 67–90, 1996.

[3] T. Xie *et al.*, "Detection of tumorigenesis in urinary bladder with optical coherence tomography: Optical characterization of morphological changes," *Opt. Exp.*, vol. 10, no. 24, p. 1431, 2002.

[4] G. A. Losa and C. Castelli, "Nuclear patterns of human breast cancer cells during apoptosis: Characterisation by fractal dimension and co-occurrence matrix statistics," *Cell Tissue Res.*, vol. 322, no. 2, pp. 257–267, 2005.

[5] M. Colombi *et al.*, "Quantitative Evaluation of mRNAs byIn SituHybridization and Image Analysis: Principles and Applications," *DNA Cell Biol.*, vol. 12, no. 7, pp. 629–636, 1993.

[6] P. A. Melrose *et al.*, "Distribution and morphology of immunoreactive gonadotropin-releasing hormone (GnRH) neurons in the basal forebrain of ponies," *J. Comparative Neurol.*, vol. 339, no. 2, pp. 269–287, 1994.

[7] M. F. Villa and F. R. Amthor, "Automating the quantitative analysis of 2-D neural dendritic trees," *J. Neurosci. Methods*, vol. 56, no. 1, pp. 77–88, 1995.

[8] M. Masseroli *et al.*, "Quantitative morphology and shape classification of neurons by computerized image analysis," *Comput. Methods Programs Biomed.*, vol. 41, no. 2, pp. 89–99, 1993.

[9] K. A. Giuliano, "Dissecting the individuality of cancer cells: The morphological and molecular dynamics of single human glioma cells," *Cell Motility Cytoskeleton*, vol. 35, no. 3, pp. 237–253, 1996.

[10] C. Broglio *et al.*, "Quantitative morphological assessment of erythroblastic differentiation induced, in vitro, in human K562 leukemic cells," *Anal. Cellular Pathol., J. Eur. Soc. Anal. Cellular Pathol.*, vol. 5, no. 3, pp. 135–146, 1993.

[11] E. C. Jensen, "Overview of Live-Cell Imaging: Requirements and Methods Used," *Anatomical Record, Adv. Integrative Anatomy Evol. Biol.*, vol. 296, no. 1, pp. 1–8, 2012.

[12] E. Cukierman *et al.*, "Taking cell-matrix adhesions to the third dimension," *Science*, vol. 294, no. 5547, pp. 1708–1712, 2001.

[13] S. Liao *et al.*, "Biomimetic nanocomposites to control osteogenic differentiation of human mesenchymal stem cells," *Adv. Healthcare Mater.*, vol. 3, no. 5, pp. 737–751, 2014.

[14] S. J. Florczyk *et al.*, "Evaluation of three-dimensional porous chitosan–alginate scaffolds in rat calvarial defects for bone regeneration applications," *J. Biomed. Mater. Res. A*, vol. 101, no. 10, pp. 2974–2983, 2013.

[15] K. Chatterjee *et al.*, "The effect of 3D hydrogel scaffold modulus on osteoblast differentiation and mineralization revealed by combinatorial screening," *Biomaterials*, vol. 31, no. 19, pp. 5051–5062, 2010.

[16] D. Chen *et al.*, "Machine learning based methodology to identify cell shape phenotypes associated with microenvironmental cues," *Biomaterials*, vol. 104, pp. 104–118, 2016.

[17] R. McBeath *et al.*, "Cell shape, cytoskeletal tension, and RhoA regulate stem cell lineage commitment," *Dev. Cell*, vol. 6, no. 4, pp. 483–495, 2004.

[18] K. A. Kilian *et al.*, "Geometric cues for directing the differentiation of mesenchymal stem cells," *Proc. Nat. Acad. Sci.*, vol. 107, no. 11, pp. 4872–4877, 2010.

[19] C. S. Chen *et al.*, "Geometric control of cell life and death," *Science*, vol. 276, no. 5317, pp. 1425–1428, 1997.

[20] S. Florczyk *et al.*, "A bioinformatics 3D cellular morphotyping strategy for assessing biomaterial scaffold niches," *ACS Biomater. Sci. Eng.*, vol. 3, no. 10, pp. 2302–2313, 2017.

[21] P. Bajcsy *et al.*, "A method for the evaluation of thousands of automated 3D stem cell segmentations," *J. Microsc.*, vol. 260, no. 3, pp. 363–376, 2015.

[22] "Mass Viewer," National Institute of Standards and Technology, 2017. [Online]. Available at: https://isg.nist.gov/deepzoomweb/stemcells3d/index.html

[23] "NIST Computational Science in Metrology," National Institute of Standards and Technology, 2017. [Online]. Available at: https://isg.nist.gov/deepzoomweb/fileBrowsing/3D/

[24] B. P. Betancourt *et al.*, "Effect of the scaffold microenvironment on cell polarizability and capacitance determined by probabilistic computations," *Biomed. Mater.*, vol. 13, no. 2, 2018, Art. no. 025012.

[25] T. M. Farooque *et al.*, "Measuring stem cell dimensionality in tissue scaffolds," *Biomaterials*, vol. 35, no. 9, pp. 2558–2567, 2014.

[26] D. Juba *et al.*, "ZENO: Software for calculating hydrodynamic, electrical, and shape properties of polymer and particle suspensions," *J. Res. Nat. Inst. Stand. Technol.*, vol. 122, pp. 1–2, 2017.

[27] M. L. Mansfield *et al.*, "Intrinsic viscosity and the electrical polarizability of arbitrarily shaped objects," *Phys. Rev. E*, vol. 64, no. 6, p. 061401, 2001.

[28] K. Asami, "Low-frequency dielectric dispersion of bacterial cell suspensions," *Colloids Surf. B, Biointerfaces*, vol. 119, pp. 1–5, 2014.

[29] A. Di Biasio and C. Cametti, "Polarizability of spherical biological cells in the presence of localized surface charge distributions at the membrane interfaces," *Phys. Rev. E*, vol. 82, no. 2, 2010, Art. no. 021917.

[30] A. Di Biasio *et al.*, "Electrical polarizability of differently shaped dielectric objects in the presence of localized interfacial charge distribution: A unifying scenario," *J. Phys. D, Appl. Phys.*, vol. 46, no. 5, 2013, Art. no. 055305.

[31] J. L. Sebastian *et al.*, "Polarizability of shelled particles of arbitrary shape in lossy media with an application to hematic cells," *Phys. Rev. E*, vol. 78, no. 5, 2008, Art. no. 051905.

[32] E. Prodan *et al.*, "The dielectric response of spherical live cells in suspension: An analytic solution," *Biophys. J.*, vol. 95, no. 9, pp. 4174–4182, 2008.

[33] J. L. Sebastian *et al.*, "Polarizability of red blood cells with an anisotropic membrane," *Phys. Rev. E*, vol. 81, no. 2, 2010, Art. no. 022901.

[34] A. Sihvola *et al.*, "Polarizabilities of platonic solids," *IEEE Trans. Antennas Propag.*, vol. 52, no. 9, pp. 2226–2233, Sep. 2004.

[35] J. D. Jackson, *Classical Electrodynamics*, 3rd ed. New York, NY, USA: Wiley, 2012.

[36] A. H. Sihvola, *Electromagnetic Mixing Formulas and Applications (IEE Electromagnetic Wave Series)*, 47 ed. London, U.K.:IET, 1999.

[37] F. Vargas Lara *et al.*, "Intrinsic conductivity of carbon nanotubes and graphene sheets having a realistic geometry," *The J. Chem. Phys.*, vol. 143, no. 20, 2015, Art. no. 204902.

[38] "COMSOL Multiphysics v. 5.2," COMSOL AB, Stockholm, Sweden, 2015.

[39] "COMSOL Multiphysics AC/DC Module User's Guide," COMSOL AB, Stockholm, Sweden, pp. 75–84, 2015.

[40] P. Cignoni *et al.*, "MeshLab: An Open-Source Mesh Processing Tool," in *Proc. Eurographics Italian Chapter Conf.*, The Eurographics Association, 2008, pp. 129–136.

[41] M. H. Reid and S. G. Johnson, "Efficient computation of power, force, and torque in BEM scattering calculations," *IEEE Trans. Antennas Propag.*, vol. 63, no. 8, pp. 3588–3598, 2015.

[42] C. Geuzaine and J.-F. Remacle, "Gmsh: A 3-D finite element mesh generator with built-in pre-and post-processing facilities," *Int. J. Numer. Methods Eng.*, vol. 79, no. 11, pp. 1309–1331, 2009.

[43] E. J. Garboczi, "Finite element and finite difference programs for computing the linear electric and elastic properties of digital images of random materials," NIST Internal Report 6269, 1998.

[44] E. Garboczi and J. Douglas, "Intrinsic conductivity of objects having arbitrary shape and conductivity," *Phys. Rev. E*, vol. 53, no. 6, p. 6169, 1996.

[45] E. J. Garboczi, "The influence of particle shape on the results of the electrical sensing zone method as explained by the particle intrinsic conductivity," *Powder Technol.*, vol. 322, pp. 32–40, 2017.

[46] A. N. Chiaramonti *et al.*, "Quantifying the 3-Dimensional shape of lunar regolith particles using X-Ray computed tomography and scanning electron microscopy at Sub-λ resolution," *Microsc. Microanal.*, vol. 23, pp. 2194–2195, 2017.

[47] D. B. Davidson, *Computational Electromagnetics for RF and Microwave Engineering*, 2nd ed. Cambridge, NY, USA: Cambridge Univ. Press, 2011.

[48] J. F. Douglas and E. J. Garboczi, "Intrinsic viscosity and the polarizability of particles having a wide range of shapes," *Adv. Chem. Phys.*, vol. 91, pp. 85–154, 1995.

[49] D. J. Audus *et al.*, "Interplay of particle shape and suspension properties: A study of cube-like particles," *Soft Matter*, vol. 11, no. 17, pp. 3360–3366, 2015.

[50] M. L. Mansfield and J. F. Douglas, "Improved path integration method for estimating the intrinsic viscosity of arbitrarily shaped particles," *Phys. Rev. E*, vol. 78, no. 4, p. 046712, 2008.

[51] L. G. Khachiyan, "Rounding of polytopes in the real number model of computation," *Math. Oper. Res.*, vol. 21, no. 2, pp. 307–320, 1996.

[52] N. Moshtagh, "Minimum volume enclosing ellipsoid," *Convex Optim.*, vol. 111, 2005, Art. no. 112.

[53] R. Pethig, "Dielectrophoresis: Status of the theory, technology, and applications," *Biomicrofluidics*, vol. 4, no. 2, 2010, Art. no. 022811.

[54] F. F. Becker *et al.*, "Separation of human breast cancer cells from blood by differential dielectric affinity," *Proc. Nat. Acad. Sci.*, vol. 92, no. 3, pp. 860–864, 1995.

[55] J. Regtmeier *et al.*, "Dielectrophoretic trapping and polarizability of DNA: The role of spatial conformation," *Anal. Chem.*, vol. 82, no. 17, pp. 7141–7149, 2010.

[56] A. Ramos *et al.*, "Ac electrokinetics: A review of forces in microelectrode structures," *J. Phys. D, Appl. Phys.*, vol. 31, no. 18, 1998, Art. no. 2338.

[57] P. R. Gascoyne and J. Vykoukal, "Particle separation by dielectrophoresis," *Electrophoresis*, vol. 23, no. 13, pp. 1973–1983, 2002.

[58] H. Morgan *et al.*, "Separation of submicron bioparticles by dielectrophoresis," *Biophys. J.*, vol. 77, no. 1, pp. 516–525, 1999.

[59] P. R. Gascoyne *et al.*, "Isolation of rare cells from cell mixtures by dielectrophoresis," *Electrophoresis*, vol. 30, no. 8, pp. 1988–1398, 2009.

[60] B. Valic *et al.*, "Effect of electric field induced transmembrane potential on spheroidal cells: theory and experiment," *Eur. Biophys. J.*, vol. 32, no. 6, pp. 519–528, 2003.

[61] T. Kotnik *et al.*, "Cell membrane electroporation-Part 1: The phenomenon," *IEEE Elect. Insul. Mag.*, vol. 28, no. 5, pp. 14–23, Sep./Oct. 2012.

[62] B. Ghanbarian and H. Daigle, "Permeability in two-component porous media: Effective-medium approximation compared with lattice-Boltzmann simulations," *Vadose Zone J.*, vol. 15, no. 2, pp. 1–10, 2016.